UC Irvine

UC Irvine Previously Published Works

Title

Hybrid Monte Carlo estimators for multilayer transport problems.

Permalink

https://escholarship.org/uc/item/3m4979pn

Authors

Zhao, Shuang
Spanier, Jerome

Publication Date

2021-04-01

DOI

10.1016/j.jcp.2021.110117

Copyright Information

Peer reviewed

Hybrid Monte Carlo estimators for multilayer transport problems

Shuang Zhao[a], **Jerome Spanier**[b,*]

[a]Computer Science Department, University of California, Irvine, United States of America

[b]Beckman Laser Institute, University of California, Irvine, United States of America

Abstract

This paper introduces a new family of hybrid estimators aimed at controlling the efficiency of Monte Carlo computations in particle transport problems. In this context, efficiency is usually measured by the figure of merit (FOM) given by the inverse product of the estimator variance $\mathrm{Var}[\xi]$ and the run time T: $\mathrm{FOM} := (\mathrm{Var}[\xi]\ T)^{-1}$. Previously, we developed a new family of transport-constrained unbiased radiance estimators (T-CURE) that generalize the conventional collision and track length estimators [1] and provide 1–2 orders of magnitude additional variance reduction. However, these gains in variance reduction are partly offset by increases in overhead time [2], lowering their computational efficiency. Here we show that combining T-CURE estimation with conventional terminal estimation *within* each individual biography can moderate the efficiency of the resulting "hybrid" estimator without introducing bias in the computation. This is achieved by treating only the refractive interface crossings with the extended next event estimator, and all others by standard terminal estimators. This is because when there are index-mismatched interfaces between the collision location and the detector, the T-CURE computation rapidly becomes intractable due to the large number of refractions and reflections that can arise. We illustrate the gains in efficiency by comparing our hybrid strategy with more conventional estimation methods in a series of multi-layer numerical examples.

Keywords

Light transport; Monte Carlo; Next-event estimation

1. Introduction

When performing a Monte Carlo simulation, it is not uncommon that the application of variance reduction strategies also produces increased computational costs. The overall impact on the figure of merit

$$\mathrm{FOM} = \frac{1}{\sigma^2 T},\tag{1}$$

is then unclear. An example of this occurs when one introduces weights in generating photon biographies and replaces absorption by weight reduction, either discrete or continuous [3]. Disallowing absorption in favor of multiplying the weight by the survival fraction μ_s/μ_t (where μ_s and μ_t denote, respectively, the scattering and extinction coefficients) clearly increases the number of collisions of each biography, hence the total processing time. The interplay between this increase in overhead and any possible reduction in the variance of the (weighted) estimator of the measurements then determines which technique is preferred in the implementation.

The example that drew our attention to this interplay involves solving 3D multi-layer problems with mismatched refractive indices at the layer interfaces. Specifically, throughout this paper we consider the problem of simulating the transport of light in multiple flat layers with varying indices of refraction. Without loss of generality, let there be m layers with the i-th layer given by

$$\mathcal{V}_i := \left\{ (x, y, z) \in \mathbb{R}^3 \mid x, y \in \mathbb{R}, z \in (z_i, z_{i+1}) \right\}, \tag{2}$$

where z_j indicates the location of the j-th interface

$$\mathcal{I}_j := \left\{ (x, y, z_j) \in \mathbb{R}^3 \mid x, y \in \mathbb{R} \right\}, \tag{3}$$

for all $j = 1, 2, \ldots, m + 1$. Under this configuration, the full medium $\mathcal{V}$ and its boundaries $\partial \mathcal{V}$ are respectively given by

$$\mathcal{V} = \bigcup_{j=1}^{m+1} \mathcal{I}_j \cup \left(\bigcup_{i=1}^{m} \mathcal{V}_i, \right), \tag{4}$$

$$\partial \mathcal{V} = \bigcup_{j=1}^{m+1} \mathcal{I}_j. \tag{5}$$

Optically, we assume each layer $\mathcal{V}_i$ to have spatially invariant optical properties and each interface $\mathcal{I}_j$ to be smooth dielectric. We provide precise mathematical descriptions for these configurations in §3.2.

Computational challenge

Previous methods leveraging next-event estimation (e.g., our transport-constrained unbiased radiance estimators (T-CURE) [2]) tally on individual collisions to lower the variance. Doing so, on the other hand, also increases the computational overhead because of the need to compute the estimator contributions from *every* collision. Nevertheless, this combination usually does increase the overall computational efficiency if one does not need to simulate the effect of *both* reflection and refraction at the layer interfaces. With the presence of refractive interfaces, however, the advantage of next-event estimation (over terminal) diminishes. This is because tallying while accounting for the Fresnel relations and refraction (according to Snell's law) at the layer interfaces can lead to many volumetric and interfacial collisions, making the tallying process extremely expensive, if not impractical. It was this

issue that sparked our interest in the use of a mixture of estimators, such as extended next-event and terminal, for estimating radiometric measurements in multiple layers with mismatching refractive interfaces.

2. Prior work

As far as the authors are aware, it was Booth and Pederson who first considered the possibility of using combinations of non-analog estimators, each of which is unbiased, for variance reduction in Monte Carlo transport simulations [4]. Their analysis relies on arguments that such estimators preserve the expected weight (tally) produced from a purely analog simulation. We have pursued a different path to the new hybrid estimators in our paper.

In what follows, we trace the development of a set of increasingly sophisticated collision-based estimators that form the basis for our new hybrid estimator (Section 4). We will use the book by Spanier and Gelbard [1] as our primary reference among others [5–9].

The general problem we consider is the estimation of radiometric measurements that capture responses of virtual detectors. The first solution to this problem is the classical collision estimator that utilizes the probability measure induced by the analog random walk process where photons travel in straight lines before being absorbed or scattered by surrounding media. It has been shown (Theorem 3.5 in the book [1]) that the collision estimator is unbiased, meaning that its expected values equal the true radiometric measurements.

The collision estimator is one of three basic transport estimators with the other two being the terminal and the track-length estimators (see Sections 2.5 and 2.6 of the book [1]). Closely related to the collision estimator, as discussed in Section 3.6 of the book [1], is the expected-value estimator which anticipates possible collisions in the regions along the direction of the photon prior to any actual collision. Expected-value estimators only produce tallies after a new direction is determined following a scattering event.[1] On the other hand, given the formula for the single-scattering phase function, one can also utilize the probability density of scattering through any angle in calculating a tally. This leads to next-event estimators, including our T-CURE estimator [2], which are capable of significantly reducing the variance and increasing the figure of merit.

Additionally, a path integral framework has been established in a few works in applied physics [1] and computer graphics [10,11]. Under this framework, the radiometric measurements are formulated as integrals of full photon biographies, and the numerical estimation of these integrals can be done using Monte Carlo integration with importance sampling. In fact, all the aforementioned estimators can be treated as importance sampling methods under the path integral framework (with different biography-sampling strategies). In this paper, we base the derivation of our hybrid estimator upon this formulation.

---

[1] Using expected value estimators to define, e.g., flux at a point, would introduce a $1/s^2$ singularity with s being the distance from a point outside the detector to one within the detector (see Spanier and Gelbard's book [1], pp. 107–110, especially Eq. (3.6.23)).

Lastly, several techniques—which are largely orthogonal to ours—have been introduced to reduce the variance of Monte Carlo estimators for solving radiative transfer problems. For example, the DXTRAN estimator available in the MCNP code [12] is used to increase the sampling in a spherical region that would otherwise be inadequately sampled (because the probability of scattering towards the region is very small). This method can introduce large weight fluctuations between particles colliding just before the sphere and particles colliding after crossing the sphere. This difficulty can be partly mitigated by extending the DXTRAN sphere to a set of nested DXTRAN spheres.

In what follows, we briefly revisit the path integral formulation in Section 3 and re-derive the collision and next-event estimators based on this formulation.

3. Overview and mathematical preliminaries

Radiative transport is the physical model that describes light propagation in scattering media ranging from human tissue to cosmic nebulae and galaxies. At the core of this formulation are the radiative transport equations involving three independent spatial variables, two for the unit direction vector, and one for time (in the time-dependent case). We refer the reader to our prior work [13] for detailed discussions of these equations.

In this paper, we focus on media with no internal light sources. In this case, for a medium enclosed in $\mathcal{V} \subseteq \mathbb{R}^3$ with boundary $\partial\mathcal{V}$, the radiance field Φ produced by a monoenergetic light source inside the medium is governed by *the integral radiative transfer equation* (IRTE):

$$\Phi(\boldsymbol{r},\,\boldsymbol{\omega}) = \int_0^{s_{\partial\mathcal{V}}} \tau(\boldsymbol{r}',\boldsymbol{r}) \left[\mu_s(\boldsymbol{r}') \int_{\mathbb{S}^2} f_p(\boldsymbol{r}',\boldsymbol{\omega}',\omega)\Phi(\boldsymbol{r}',\boldsymbol{\omega}')\mathrm{d}\boldsymbol{\omega}' \right] \mathrm{d}s \qquad (6)$$
$$+ \tau(\boldsymbol{r}_{\partial\mathcal{V}},\boldsymbol{r})\phi(\boldsymbol{r}_{\partial\mathcal{V}},\boldsymbol{\omega}),$$

where

- μ_t is the *total attenuation*, or *extinction*, coefficient;

- μ_s is the *scattering* coefficient;

- f_p is the *single-scattering phase function*;

- $s_{\partial\mathcal{V}}$ denotes the minimal distance between $\boldsymbol{r}$ and a point on the medium boundary $\partial\mathcal{V}$ via direction $-\boldsymbol{\omega}$.[2] Namely, $s_{\partial\mathcal{V}} := \inf\{s \mid \boldsymbol{r} - s\boldsymbol{\omega} \in \partial\mathcal{V}\}$;

- $\boldsymbol{r}' := \boldsymbol{r} - s\boldsymbol{\omega}$, $\boldsymbol{r}_{\partial\mathcal{V}} := \boldsymbol{r} - s_{\partial\mathcal{V}}\boldsymbol{\omega}$, and $\tau(\boldsymbol{r}',\boldsymbol{r})$ denotes the *transmittance* between $\boldsymbol{r}'$ and $\boldsymbol{r}$ given by a line integral over the segment $\overline{\boldsymbol{r}'\boldsymbol{r}}$:

---

[2]In case of an infinite medium, $s_{\partial\mathcal{V}}$ can sometimes be infinite, causing the second term on the right-hand side of Eq. (6) to vanish.

$$\tau(\boldsymbol{r}', \boldsymbol{r}) = \exp\left(-\int_{\boldsymbol{r}'\boldsymbol{r}} \mu_t(\boldsymbol{x})\mathrm{d}\boldsymbol{x}\right); \tag{7}$$

- ϕ denotes the incident radiance at the medium boundary and acts as the boundary condition of the system.

In discussing light transport in turbid media, the IRTE (6) is sometimes expressed in terms of transformed dependent variables:

$$\Phi(\boldsymbol{P}) = \int_0^{s_{\partial\mathcal{V}}} \int_{\mathbb{S}^2} K(\boldsymbol{P}' \to \boldsymbol{P})\Phi(\boldsymbol{P}')\mathrm{d}\boldsymbol{\omega}'\mathrm{d}s + S(\boldsymbol{P}), \tag{8}$$

where $\boldsymbol{P} := (\boldsymbol{r}, \boldsymbol{\omega})$, $\boldsymbol{P}' := (\boldsymbol{r}', \boldsymbol{\omega}') \in V \times \mathbb{S}^2$, and

$$K(\boldsymbol{P}' \to \boldsymbol{P}) := \mu_S(\boldsymbol{r}')f_p(\boldsymbol{r}', \boldsymbol{\omega}', \boldsymbol{\omega})\tau(\boldsymbol{r}', \boldsymbol{r}), \tag{9}$$

$$S(\boldsymbol{P}) := \tau(\boldsymbol{r}_{\partial\mathcal{V}}, \boldsymbol{r})\phi(\boldsymbol{r}_{\partial\mathcal{V}}, \boldsymbol{\omega}). \tag{10}$$

Handling reflective/refractive interfaces

Many real-world problems involve multiple media separated by interfaces interacting with light via reflection and refraction. In this case, light transport in each medium is governed by an IRTE (6), (8), and the system of equations is further coupled by a set of interface equations of the form

$$\phi(\boldsymbol{r}, \boldsymbol{\omega}) = \int_{\mathbb{S}^2} \Phi_i(\boldsymbol{r}, \boldsymbol{\omega}')f_s(\boldsymbol{r}, \boldsymbol{\omega}', \boldsymbol{\omega})\mathrm{d}\sigma(\boldsymbol{\omega}') + \phi_e(\boldsymbol{r}, \boldsymbol{\omega}), \tag{11}$$

where $\Phi_i(\boldsymbol{r}, \boldsymbol{\omega}')$ denotes the incident radiance from either side of the interface and equals $\Phi(\boldsymbol{r}, -\boldsymbol{\omega}')$ given by the corresponding IRTE. Further, f_s depicts the surface scattering profile, σ denotes the measure of projected solid angle, and ϕ_e is the (known) source term capturing light emitted at the medium interfaces.

Radiometric measurements

In many applications, one is concerned with some *radiometric measurement I* given by the inner product between the interfacial radiance ϕ and some *measurement function* W_e (that usually specifies the physical dimensions of a radiometric detector):

$$I = \langle W_e, \phi \rangle := \int_{\partial\mathcal{V}} \int_{\mathbb{S}^2} W_e(\boldsymbol{r}, \boldsymbol{\omega})\phi(\boldsymbol{r}, \boldsymbol{\omega})\, \mathrm{d}\sigma(\boldsymbol{\omega})\, \mathrm{d}\boldsymbol{r}. \tag{12}$$

For instance, to measure the radiance at some fixed location $r_0 \in \mathcal{V}$ with direction $\omega_0 \in \mathbb{S}^2$, one can set $W_e(r, \omega) = \delta(r - r_0)\, \delta(\omega - \omega_0)$ with δ being the Dirac delta function.

3.1. Path integral formulation

The measurement (12) can also be expressed as a pure integral that is usually termed the *path integral* [10,11]:

$$I = \int_{\mathcal{B}} f(\bar{b})\mathrm{d}\mu(\bar{b}), \tag{13}$$

where:

- $\mathcal{B}$ is a probability measure space (sometimes termed the *path space*) that is the sample space of all possible photon biographies $\bar{b}$.

- μ is a probability measure (sometimes termed the *throughput measure*) on $\mathcal{B}$. For any photon biography $\bar{b} = (r_0, r_1, ..., r_K)$, $\mathrm{d}\mu(\bar{b})$ is given by

$$\mathrm{d}\mu(\bar{b}) = \prod_{k=0}^{K} \mathrm{d}r_k, \tag{14}$$

  where $\mathrm{d}r_k$ has area measure if $r_k \in \partial\mathcal{V}$ and volume measure if $r_k \in \mathcal{V} \backslash \partial\mathcal{V}$.

- $f : \mathcal{B} \to \mathbb{R}$ describes the contribution (aka. throughput) of any photon biography (aka. light transport path) $\bar{b}$ to the radiometric detector. For any photon biography $\bar{b} = (r_0, ..., r_K)$, let ω_k denote the direction from r_k to r_{k+1} (i.e., $\omega_k = (r_{k+1} - r_k)/\|r_{k+1} - r_k\|$) for $k = 0, 1, ..., K - 1$. Then, the contribution $f(\bar{b})$ has been demonstrated to equal the product of per-vertex terms v_k and per-segment terms s_k [11]

$$f(\bar{b}) = \left(\prod_{k=0}^{K} v_k\right)\left(\prod_{k=1}^{K} s_k\right). \tag{15}$$

  Specifically, the per-vertex contributions v_k are given by

$$V_k = \begin{cases} \phi_e(r_0, \omega_0), & k = 0, \\ W_e(r_K, \omega_{K-1}), & k = K \\ f_s(r_k, \omega_{k-1}, \omega_k), & 0 < k < K, r_k \in \partial\mathcal{V}, \\ \mu_s(r_k) f_p(r_k, \omega_{k-1}, \omega_k), & 0 < k < K, r_k \in \mathcal{V} \backslash \partial\mathcal{V}, \end{cases} \tag{16}$$

  where ϕ_e and W_e describe the emission of the source and the response of the detector, respectively. The per-segment contributions s_k equal

$$s_k = \hat{\tau}(r_{k-1}, r_k)\frac{|\langle n(r_{k-1}), \omega_{k-1}\rangle| \cdot |\langle n(r_k), \omega_{k-1}\rangle|}{\|r_k - r_{k-1}\|^2}, \tag{17}$$

where $\hat{\tau}$ is the visibility-aware transmittance (which equals the transmittance τ between $\boldsymbol{r}_{k-1}$ and $\boldsymbol{r}_k$ if the two points are mutually visible, and zero otherwise) and $\boldsymbol{n}$ denotes interface normal directions. Note that, for those $\boldsymbol{r}_{k-1}$ and $\boldsymbol{r}_k$ representing volumetric collisions, the corresponding inner product terms are simply set to one.

3.2. Problem specification

As stated in §1, we consider in this paper the problem of simulating light transport in multiple flat layers with varying indices of refraction. The layers $\{\mathcal{V}_i\}$ and interfaces $\{\mathcal{I}_j\}$ are defined in Eqs. (2), (3), respectively.

Optically, we assume each layer $\mathcal{V}_i$ to have spatially invariant extinction coefficient $\sigma_t^{(i)}$, scattering coefficient $\sigma_s^{(i)}$, phase function $f_p^{(i)}$, and each interface $\mathcal{I}_j$ to be smooth dielectric with the scattering function

$$f_s(\boldsymbol{\omega}', \boldsymbol{\omega}) = F_t \frac{\delta(\boldsymbol{\omega}' - \boldsymbol{\omega}_t)}{|\cos \boldsymbol{\omega}'|} + (1 - F_t)\frac{\delta(\boldsymbol{\omega}' - \boldsymbol{\omega}_r)}{|\cos \boldsymbol{\omega}'|}, \tag{18}$$

where $\boldsymbol{\omega}_t$ and $\boldsymbol{\omega}_r$ denote the reflected and refracted directions of $\boldsymbol{\omega}$, F_t denotes the Fresnel transmittance term, and $\cos \boldsymbol{\omega}'$ indicates the inner product between $\boldsymbol{\omega}'$ and the layer normal $[0, 0, 1]$. With this scattering profile, the interface equations (11) reduce to

$$\phi(\boldsymbol{r}, \boldsymbol{\omega}) = F_t \Phi_i(\boldsymbol{r}, \boldsymbol{\omega}_t) + (1 - F_t)\Phi_i(\boldsymbol{r}, \boldsymbol{\omega}_r), \tag{19}$$

for all $\boldsymbol{r} \in \partial\mathcal{V}$ and $\boldsymbol{\omega} \in \mathbb{S}^2$.

3.3. Monte Carlo solutions

Under our problem specification, the radiometric measurements (12), (13) have no closed-form solution. Instead, we rely on Monte Carlo integration (with importance sampling) to estimate them. Specifically, assume p to be a probability density function over the path space $\mathcal{B}$ such that $p(\bar{\boldsymbol{b}}) > 0$ whenever $f(\bar{\boldsymbol{b}}) > 0$. Let $\bar{\boldsymbol{b}}_1, ..., \bar{\boldsymbol{b}}_N \in \mathcal{B}$ be sample biographies drawn independently from p. Then, it holds that

$$\frac{1}{N}\sum_{n=1}^{N}\frac{f(\bar{\boldsymbol{b}}_n)}{p(\bar{\boldsymbol{b}}_n)} N \to \infty \int_{\mathcal{B}} f(\bar{\boldsymbol{b}})\mathrm{d}\mu(\bar{\boldsymbol{b}}) = I . \tag{20}$$

In other words, the left-hand side of Eq. (20) is a **theoretically unbiased** estimator of I.

Previously, several types of transport estimators have been developed. A classical *terminal* estimator, which has been implemented by many software libraries such as MCML [14], randomly constructs photon biographies by directly simulating the underlying analog stochastic process. A *next-event* estimator, in contrast, tallies at individual collisions to reduce estimation variance. Both estimators can be derived in multiple mathematically equivalent ways. We now provide brief derivations for both of them using the path integral framework (13), (20).

Besides terminal and next-event, *collision* and *track-length* estimators have also been introduced to estimate volumetric properties such as collision density [1]. As we are concerned with radiometric measurements provided by detectors located on layer interfaces (as expressed in Eq. (12)), we will focus on the terminal and next-event estimators (as well as their extensions) in the rest of this paper.

Terminal estimator—This estimator works by directly simulating the standard *analog* procedure, a Markov process. Specifically, a photon starts with a location $r_0 \in \partial\mathcal{V}$ on the source with an initial direction ω_0. Then, the photon interacts with the surrounding media and interfaces by (i) traveling straight for a random *free-flight distance* $\tau_i \in \mathbb{R}_+$; (ii) colliding with the medium or an interface at $r_{i+1} = r_i + \tau_i\omega_i$; and (iii) switching to a random new direction ω_{i+1} based on the phase function of the medium or the scattering profile of the interface. This process is repeated for $i = 0, 1, \ldots$ until reaching the detector at some r_K. In this way, the probability density for constructing an entire photon biography $\bar{b} = (r_0, r_1, \ldots, r_K)$ is

$$p^{\text{terminal}}(\bar{b}) = p(r_0)\prod_{k=0}^{K-1} p(r_{k+1} \mid r_k),\tag{21}$$

where $p(r_{k+1} \mid r_k)$ captures the probability for the photon to take direction $\omega_k \in \mathbb{S}^2$ and free-flight distance $\tau_k = \|r_{k+1} - r_k\|$ at r_k. Given Eq. (21), the terminal estimator can be obtained via

$$\frac{f(\bar{b})}{p^{\text{terminal}}(\bar{b})} = \frac{\left(\prod_{k=0}^{K} v_k\right)\left(\prod_{k=1}^{K} s_k\right)}{p^{\text{terminal}}((r_0, \ldots, r_K))} = \frac{C_0}{p(r_0)}\left(\prod_{\substack{1 \le k < K, \\ r_K \in \mathcal{V}\backslash\partial\mathcal{V}}} \alpha_k\right) W_e(r_K, \omega_{K-1}),\tag{22}$$

where the vertex v_k and segment s_k contributions are respectively given by Eqs. (16), (17), $\alpha_k := \mu_s^{(k)}/\mu_t^{(k)}$ is the single-scattering albedo at r_k, and c_0 is a normalization constant. Please refer to Appendix A for a detailed derivation.

Next-event estimation—Although conceptually simple, the terminal estimator converges slowly when the chance for a photon to randomly hit the radiometric detector is low. This happens when the detector is placed distantly from the source or has small surface area. To address this problem, a new family of methods, including our T-CURE estimator [2], has been introduced. These estimators leverage a technique called *next-event estimation*. Unlike the terminal estimator, next-event estimation tallies at every vertex of a photon biography and usually leads to faster convergence.

When applied to the multi-layer problem with dielectric interfaces, since the interfacial collisions are "specular" (i.e., involving Dirac delta functions), tallying occurs at volumetric collisions in the interior of layers adjacent to the detector (which is assumed to be located on an interface). In this way, a photon biography $\bar{b} = (r_0, \ldots, r_K)$ with $r_{K-1} \in \mathcal{V}\backslash\partial\mathcal{V}$ is

constructed by having the prefix $\bar{b}' := (r_0, ..., r_{K-1})$ generated the same way as the terminal estimator and the last vertex r_K sampled from the surface of the detector uniformly, leading to the probability density:

$$p^{\text{NE}}(\bar{b}) = p^{\text{terminal}}(\bar{b}')p(r_K), \quad (23)$$

where $p^{\text{terminal}}(\bar{b}')$ follows Eq. (22), and $p(r_K) = 1/|\mathscr{D}|$ with $|\mathscr{D}|$ indicating the surface area of the detector. Since $f(\bar{b}) = f(\bar{b}')s_K v_K$ where s_K and v_K are respectively the contributions of the K-th segment and vertex given by Eqs. (16), (17), we have

$$\begin{aligned}
\frac{f(\bar{b})}{p^{\text{NE}}(\bar{b})} &= \frac{f(\bar{b}')}{p^{\text{terminal}}(\bar{b}')}\frac{s_K v_K}{p(r_K)} \\
&= \frac{f(\bar{b}')}{p^{\text{terminal}}(\bar{b}')}|\mathscr{D}|W_e(r_K, \omega_{K-1})\hat{\tau}(r_{K-1}, r_K)\frac{\cos\omega_{K-1}}{\|r_K - r_{K-1}\|^2}.
\end{aligned} \quad (24)$$

In practice, during one random walk process, a next-event estimator effectively constructs multiple (correlated) photon biographies. In other words, every time the estimator tallies using Eq. (24), an effective photon biography is generated.

4. Our method

4.1. Hybrid estimators

Our method is built upon a general framework that allows multiple estimators to be used jointly to estimate radiometric measurements (12). Specifically, assume that the path space $\mathscr{B}$ can be partitioned into L disjoint sub-domains $\mathscr{B}_1, \mathscr{B}_2, ..., \mathscr{B}_L$, yielding

$$I = \sum_{l=1}^{L}\int_{\Omega_l} f(\bar{b})\mathrm{d}\mu(\bar{b}). \quad (25)$$

Further, for each l, let p_k be a biography-constructing probability density satisfying that $p_l(\bar{b}) > 0$ whenever $f(\bar{b}) > 0$ for all $\bar{b} \in \mathscr{B}_l$. Then, it is easy to verify that

$$\langle I \rangle_{\text{hybrid}} := \sum_{l=1}^{L}\frac{f(\bar{b}_l)\chi[\bar{b}_l \in \mathscr{B}_l]}{p_l(\bar{b}_l)}, \quad (26)$$

is an unbiased estimator of I where $\bar{b}_l$ is a biography drawn from p_l and χ denotes the indicator function (which equals one when the specified condition is satisfied and zero otherwise). Since $\langle I \rangle_{\text{hybrid}}$ leverages multiple estimators, we term it an *hybrid estimator* of I.

Remark—Under the framework presented in Eq. (26), each component estimator only needs to handle one class of biographies (i.e., those from $\mathscr{B}_l$ for each l). Thus, it is all right for the l-th estimator to neglect (i.e., never sample) a biography $\bar{b}$ with $f(\bar{b}) > 0$ as long as $\bar{b} \notin \mathscr{B}_l$. This additional flexibility enables new possibilities for the design of efficient estimators, which we will demonstrate in the rest of this paper.

Our hybrid estimator—In what follows, we introduce a new estimator to solve the problem of light transport in index-mismatching layers following the hybrid framework depicted in Eq. (26). Specifically, we set $L = 2$:

$$\langle I \rangle_{\text{ours}} = \frac{f(\bar{\boldsymbol{b}}_1)\chi\left[\bar{\boldsymbol{b}}_1 \in \mathscr{B}_1\right]}{p_1(\bar{\boldsymbol{b}}_1)} + \frac{f(\bar{\boldsymbol{b}}_2)\chi\left[\bar{\boldsymbol{b}}_2 \in \mathscr{B}_2\right]}{p_2(\bar{\boldsymbol{b}}_2)},$$

(27)

and use p_1 given by our new next-event-like process capable of crossing layer boundaries (§4.2) and p_2 by the standard terminal estimator. Our new estimator is unbiased and much more efficient than traditional terminal and next-event estimators, which will be demonstrated empirically in §5.

In the rest of this section, we provide a detailed description of our new hybrid estimator.

4.2. Extended next-event estimation

The core of our hybrid estimator is an extended next-event estimation technique capable of crossing multiple interface boundaries. Similar to traditional next-event estimation, we would like to directly connect to the detector from every volumetric collision.[3] To do this efficiently under the multi-layer configuration depicted in §3.2, we need to allow the connection to contain surface interactions (i.e., reflection and refraction), as demonstrated in Fig. 1. Since a connection can involve arbitrarily many such interactions, there exist infinitely many valid connections.

To make our extended next-event estimation tractable, we consider next-event connections *with refraction only* (e.g., Fig. 1–a) while leaving all other possibilities (e.g., Fig. 1–bc) to be handled with a standard terminal estimator using the hybrid framework (§4.1).

Path-space partitioning—Precisely, we partition the path space $\mathscr{B}$ into two subdomains $\mathscr{B}_1$ and $\mathscr{B}_2$ as follows. Let $\bar{\boldsymbol{b}} = (\boldsymbol{r}_0, \boldsymbol{r}_1, ..., \boldsymbol{r}_K)$ be an arbitrary photon biography (with $\boldsymbol{r}_0$, $\boldsymbol{r}_k \in \partial\mathscr{V}$ respectively located on the source and the detector). Then, $\bar{\boldsymbol{b}} \in \mathscr{B}_1$ if and only if there exists some $k \in \{1, 2, ..., K-1\}$ satisfying: (i) $\boldsymbol{r}_k$ corresponds to a volumetric collision; and (ii)$\boldsymbol{r}_{k+1}, \boldsymbol{r}_{k+2}, ..., \boldsymbol{r}_{K-1}$ all correspond to interfacial refraction.

Based on this partitioning, we use: (i) an extended next-event estimator to efficiently handle photon biographies from $\mathscr{B}_1$; and (ii) a standard terminal estimator for $\mathscr{B}_2 = \mathscr{B}\backslash\mathscr{B}_1$.

Extended next-event connection—Given an internal collision at location $\boldsymbol{r} \in \mathscr{V}\backslash\partial\mathscr{V}$, we aim to draw $\boldsymbol{\omega} \in \mathbb{S}^2$ such that extending a light ray with origin $\boldsymbol{r}$ and direction $\boldsymbol{\omega}$ (while refracting through layer boundaries) can eventually hit the detector at $\mathscr{D} \subseteq \partial\mathscr{V}$. Notice that with smooth dielectric interfaces, the extension of a light ray is deterministic given $\boldsymbol{r}$ and $\boldsymbol{\omega}$.

Similar to traditional next-event estimation methods, we draw a point $\boldsymbol{r}_d$ on the detector $\mathscr{D}$ from some predetermined probability density $p(\boldsymbol{r}_d)$ and seek $\boldsymbol{\omega}$ such that the extended

---

[3]In general, it is also desirable to connect from every interfacial scattering. This, however, is unnecessary due to our smooth surface scattering profiles (18).

light ray indeed intersects the detector at r_d. Notice that, due to the presence of refractive interfaces, setting $\boldsymbol{\omega} = (r_d - r)/\|r_d - r\|$ does not work in general. As shown in Fig. 2–a, it is easy to verify that the desired direction $\boldsymbol{\omega}$ should lie within the plane determined by r, r_d, and the normal $\boldsymbol{n}$ of all layer boundaries (recall that we assume all layers to be parallel flat slabs). Then, as illustrated in Fig. 2–b, the search for $\boldsymbol{\omega}$ amounts to finding a proper angle $\theta \in [0, \pi/2)$ such that, within the layer boundary containing $\mathcal{D}$, the distance $F(\theta)$ between the projection r' of r and the intersection of the extended light ray equals $\|r' - r_d\|$. Specifically, F is given by

$$F(\theta) = \sum_{\rho = 0}^{P} h_\rho \tan \theta_\rho, \tag{28}$$

where P denotes the number of refractive interfaces between r and the detector, θ_ρ is the angle between the normal to the light ray after ρ refractions (so $\theta_0 = \theta$), and h_ρ denotes the projected distance between the ρ-th and the $(\rho + 1)$-th vertices on the extended light ray.

According to Eq. (28), we know that F increases monotonically between 0 and ∞ when θ varies from 0 to $\pi/2$. Thus, there exists exactly one θ satisfying $F(\theta) = \|r' - r_d\|$ for any $r_d \in \mathcal{D}$. In practice, we further exploit the monotonicity of F by calculating θ using the bisection method.

Change of variable—At each internal scattering location r, we draw $\boldsymbol{\omega}$ for our extended next-event estimation by sampling $r_d \in \mathcal{D}$ and computing $\theta = F^{-1}\|r' - r_d\|$ (which in turn determines $\boldsymbol{\omega}$). To properly calculate the probability density for generating a photon biography with our extended next-event connection, we need to write down the probability p as a function of $\boldsymbol{\omega}$ (instead of r_d). Let F be the mapping from $\boldsymbol{\omega} \in \mathbb{S}^2$ to $r_d \in \mathcal{D}$. Then, the probability density of $\boldsymbol{\omega}$ based on that of r_d involves evaluating the determinant of the Jacobian $\boldsymbol{J}_{F}{}^{-1}$ of the inverse mapping $\boldsymbol{F}^{-1}$ at $\boldsymbol{\omega}$:

$$p(\boldsymbol{\omega}) = p(r_d)\left|\det(\boldsymbol{J}_{F}{}^{-1}(\boldsymbol{\omega}))\right|. \tag{29}$$

Specifically, it can be shown that

$$p(\boldsymbol{\omega}) = p(r_d)\frac{\sin\theta}{F(\theta)F'(\theta)}, \tag{30}$$

where F' denotes the first derivative of F with respect to θ. See Appendix B for more details on the derivation.

Our next-event estimator—We now provide the exact mathematical form of our next-event estimator, the key component of our hybrid estimator (27). To this end, we need to write down the probability density p_1 for photon biographies $\bar{b} \in \mathscr{B}_1$ constructed using the aforementioned extended next-event connections.

Given a photon biography $\bar{b} = (r_0, r_1, ..., r_K)$ with $r_0 \in \partial\mathcal{V}$ located on the source and $r_K \in \mathcal{D} \subseteq \partial\mathcal{V}$ on the detector, assume without loss of generality that the extended next-event

connection is performed on $r_i \in \mathcal{V} \backslash \partial \mathcal{V}$ with $0 < i < K$. It follows that, for all $i < i' < K$, $r_{i'}$ corresponds to a refraction on a layer interface. Then, it holds that the probability for drawing $\bar{b}$ equals the product of probabilities for drawing its prefix $(r_0, \ldots, r_i)$ and the extended next-event suffix $(r_{i+1}, \ldots, r_K)$ given r_i. That is,

$$p_1(\bar{b}) = p((r_0, \ldots, r_i))p((r_{i+1}, \ldots, r_K) \mid r_i). \tag{31}$$

Additionally, the measurement contribution of $\bar{b}$ given by Eq. (15) can be decomposed as

$$f(\bar{b}) = \underbrace{\left[\left(\prod_{k=0}^{i-1} \upsilon_k\right)\left(\prod_{k=1}^{i} s_k\right)\right]}_{\text{Contribution of } (r_0, \ldots, r_i)} \underbrace{\left[\left(\prod_{k=i}^{K} \upsilon_k\right)\left(\prod_{k=i+1}^{K} s_k\right)\right]}_{\text{Contribution of } (r_{i+1}, \ldots, r_K)}. \tag{32}$$

Then, the tally of our extended next-event estimator equals

$$\frac{f(\bar{b})}{p_1(\bar{b})} = \frac{\left(\prod_{k=0}^{i-1} \upsilon_k\right)\left(\prod_{k=1}^{i} s_k\right)}{p((r_0, \ldots, r_i))} \frac{\left(\prod_{k=i}^{K} \upsilon_k\right)\left(\prod_{k=i+1}^{K} s_k\right)}{p((r_{i+1}, \ldots, r_K) \mid r_i)}, \tag{33}$$

where the first factor on the RHS only depends on $(r_0, \ldots, r_i)$ and is given by Eq. (22).

We now focus on expressing the probability for building $(r_{i+1}, \ldots, r_K)$ using our extended next-event connection at r_i. Based on our change of variable result (30), this probability can be expressed as

$$p((r_{i+1}, \ldots, r_K) \mid r_i) = p(r_K)\frac{\sin\theta_i}{F(\theta_i)F'(\theta_i)}, \tag{34}$$

where θ_i is the angle between the layer normal $n = [0, 0, 1]$ and ω_i. It follows that

$$\frac{\left(\prod_{k=i}^{K} \upsilon_k\right)\left(\prod_{k=i+1}^{K} s_k\right)}{p((r_{i+1}, \ldots, r_K) \mid r_i)} = W_e(r_K, \omega_{K-1})f_p(r_i, \omega_{i-1}, \omega_i)\frac{F(\theta_i)F'(\theta_i)}{p(r_K)\sin\theta_i} \\ \left(\prod_{k=i+1}^{K-1} \tau(r_{k-1}, r_k)F_t^{(k)}\right)\tau(r_{K-1}, r_K), \tag{35}$$

where

$$\tau(r_{k-1}, r_k) = \exp(-\mu_t^{(k-1)}\|r_k - r_{k-1}\|), \tag{36}$$

captures the transmittance between r_{k-1} and r_k for all k, and $F_t^{(k)}$ denotes the Fresnel transmission at r_k.

In practice, we draw r_K uniformly on the detector for our extended next-event connection, yielding $p(r_K) \equiv 1/|\mathcal{D}|$ with $|\mathcal{D}|$ being the detector's surface area. Then, the tally function of our extended next-event estimator can be expressed as:

$$\frac{f(\bar{\boldsymbol{b}})}{p_1(\bar{\boldsymbol{b}})} = \frac{\left(\prod_{k=0}^{K} v_k\right)\left(\prod_{k=0}^{K} s_k\right)}{p((\boldsymbol{r}_0,\ldots,\boldsymbol{r}_i))p((\boldsymbol{r}_{i+1},\ldots,\boldsymbol{r}_K) \mid \boldsymbol{r}_i)}$$

$$= \frac{c_0}{p(\boldsymbol{r}_0)}\left(\prod_{\substack{1 \le k \le i, \\ \boldsymbol{r}_K \in \mathscr{V}\backslash\partial\mathscr{V}}} \alpha_k\right) W_e(\boldsymbol{r}_K, \boldsymbol{\omega}_{K-1}) f_p(\boldsymbol{r}_i, \boldsymbol{\omega}_{i-1}, \boldsymbol{\omega}_i) \qquad (37)$$

$$\frac{|\mathscr{D}|F(\theta_i)F'(\theta_i)}{\sin\theta_i}\left(\prod_{k=i+1}^{K-1} \tau(\boldsymbol{r}_{k-1},\boldsymbol{r}_k)F_t^{(k)}\right)\tau(\boldsymbol{r}_{K-1},\boldsymbol{r}_K),$$

for all $\bar{\boldsymbol{b}} \in \Omega_1$.

5. Experimental results

We implemented our hybrid estimator in C++ with multi-threading enabled using OpenMP. We demonstrate the effectiveness of our technique empirically via a few numerical experiments.

5.1. A two-layer problem

We test our technique using a layered configuration modeled after human tissue with optical properties given by prior works [15–17]. As shown in Fig. 3, our configuration involves two homogeneous layers and varying refractive indices separated by dielectric interfaces. Additionally, a pair of small disc source and detector (with 0.05 mm cross-sectional diameters and fully open apertures) are placed 2 mm away from each other.

Results—Fig. 4 compares the efficiency of the terminal and our estimators measured using figure of merit (FOM) given by Eq. (1). In this experiment, we estimate the flux received by the detector and execute both estimators multiple times (in 5, 50, 500, and 5000 seconds, respectively). As our method runs more slowly per random walk, we use fewer samples to keep the total computation times similar. Still, our hybrid estimator outperforms the terminal estimator significantly by offering an FOM that is over an order of magnitude larger.

Fig. 5 further visualizes the received flux in a directionally resolved fashion (i.e., intensity) where each direction from the lower hemisphere is projected down to a unit disc. These results are obtained using the same equal-time setting as Fig. 4 and demonstrate the capability of our hybrid method to produce significantly cleaner estimations with lower rooted mean-square error (RMSE) with respect to a reference solution computed using 10× samples as (e2).

Additionally, we show per-component visualizations of our estimated result in Fig. 6. The full estimation is shown in Fig. 6–a, which is identical to Fig. 5–d2. Recall that, as expressed in Eq. (27) in §4, our hybrid estimator partitions the path space $\mathscr{B}$ into two disjoint subsets $\mathscr{B}_1$ and $\mathscr{B}_2$. Fig. 6–b visualizes the component estimated with our extended next-event estimation using photon biographies from $\mathscr{B}_1$. Additionally, Fig. 6–c shows the estimation obtained with the terminal estimator using photon biographies from $\mathscr{B}_2$.

5.2. Beyond two layers

Our technique is capable of handling media with arbitrary numbers of layers. To demonstrate this, we conduct another experiment using a configuration with four layers with alternating properties (see Fig. 7). We visualize the estimated intensity in Fig. 8 where our technique outperforms the terminal estimator by producing cleaner estimates with much lower RMSE (as shown above each intensity visualization result).

6.   Summary and conclusions

Conclusion

In this paper, we have introduced a new family of *hybrid estimators* that combine the benefits of two or more unbiased estimators in order to increase the computational efficiency.

The prototypical problem that we study here involves a multilayer system of radiative transfer equations (6) that are coupled by a set of interface conditions (11). In estimating radiometric measurements (12) in such a system, terminal estimations can lead to large variances when the biographies rarely traverse the path from the source to detector. When the layers' refractive indices are index-matched, we showed in [13] that use of a transport-constrained unbiased radiance estimator (T-CURE) to estimate reflectance is several orders of magnitude more accurate than the terminal estimate of reflectance. This improvement is achieved because, in the absence of index-mismatched interfaces between each collision point and the detector, T-CURE can make use of the *expected* contribution to reflectance from *every* collision of *each* photon biography. However, when there are index-mismatched interfaces between the collision location and the detector, the T-CURE computation rapidly becomes intractable due to the large number of both reflections and refractions that can arise.

In §3.2, we describe a multilayer problem (2), (3) where each layer has constant optical properties and each interface is assumed to be smooth dielectric (18). §4.2 discusses our new extended next-event estimation technique that is capable of crossing multiple interface boundaries. This is accomplished by handling only refractive interface crossings with the extended next-event estimator, and all others by standard terminal estimation.

In §5, we demonstrate the gains in computational efficiency obtained by the hybrid estimator.

Future work

Our extended next-event estimation (§4.2) relies on the assumption that the layer interfaces are planar and parallel to each other. Although this is the case under the (idealized) layered configuration, generalizing to more general geometries is an interesting future topic. It is also possible to consider a number of other, potentially finer, partitions of the phase space, each of which would give rise to a new, different hybrid estimator. This is because the partitioning establishes how many reflections and refractions are permitted prior to switching to the analog estimator. An interesting optimization problem arises from such

considerations because the finer the partition, the more costly is the computation, but the additional information garnered from allowing more reflections and refractions, the smaller (in general) is the statistical uncertainty in the estimate.

Acknowledgements

Appendix A. Derivation of the terminal estimator

The construction of a photon biography $\bar{b} = (r_0, \ldots, r_K)$ using the standard analog procedure works as follows. Starting with an initial location r_0 on the source $\mathcal{S}$, the following Markov process is performed for $k = 0, 1, \ldots, K - 1$ to draw the remaining vertices.

1. Given r_k, draw a direction ω_k based on the source function ϕ_e (when $k = 0$), the interfacial scattering profile f_s (when $k > 0$ and $r_k \in \partial\mathcal{V}$), or the phase function f_p (when $k > 0$ and $r_k \in \mathcal{V}\backslash\partial\mathcal{V}$).

2. Sample a distance s_k from an exponential distribution with the parameter $\mu_t^{(k)}$ that equals the extinction coefficient of the layer containing (r_k, ω_k).

3. If the line segment connecting ω_k and $r_k + s_k\omega_k$ intersects any layer boundary (i.e., $\{r_k + s\omega_k \mid 0 < s < s_k\} \cap \partial\mathcal{V} \neq \varnothing$), update s_k by setting $s_k \leftarrow \inf\{s \mid s > 0$ and $r_k + s\omega_k \in \partial\mathcal{V}\}$.

4. Set $r_{k+1} \leftarrow r_k + s_k\omega_k$.

Since r_{k+1} only depends on r_k and r_{k-1} (when $k > 0$), the construction of photon biographies is a second-order Markov process. Precisely, $p(r_{k+1} \mid r_k)$ in Eq. (21) equals

$$p(r_{k+1} \mid r_k) = \begin{cases} p(\omega_k)\exp(-\mu_t^{(k)}s_k)\dfrac{\cos\omega_k}{\|r_{k+1} - r_k\|^2}, & (r_{k+1} \in \partial\mathcal{V}) \\ p(\omega_k)\mu_t^{(k)}\exp(-\mu_t^{(k)}s_k)\dfrac{1}{\|r_{k+1} - r_k\|^2}, & (r_{k+1} \in \mathcal{V}\backslash\partial\mathcal{V}) \end{cases} \tag{A.1}$$

where $\cos\omega_k := |\langle n, \omega_k \rangle|$ with $n = [0, 0, 1]$ being the layer normal, $\mu_t^{(k)}$ is the extinction coefficient of the layer given by r_k and ω_k, and the last factors account for the change from $d\omega_k$ and $d\omega_k ds_k$ to dr_{k+1}, respectively. In Eq. (A.1), $p(\omega_k)$ captures the probability for drawing ω_k at r_k (Step 1 above):

$$p(\omega_k) = \begin{cases} c_0^{-1}\phi_e(r_0, \omega_0)\cos\omega_0, & (k = 0) \\ f_s(r_k, \omega_{k-1}, \omega_k)\cos\omega_k, & (k > 0 \text{ and } r_k \in \partial\mathcal{V}) \\ f_p(r_k, \omega_{k-1}, \omega_k), & (k > 0 \text{ and } r_k \in \mathcal{V}\backslash\partial\mathcal{V}) \end{cases} \tag{A.2}$$

with $c_0 \in \mathbb{R}_+$ being a normalization factor.

Lastly, Eq. (22) can be obtained according to Eqs. (21), (A.1), (A.2).

Appendix B. Change of variable

In what follows, we derive the ratio between the solid angle measure ($d\sigma$) and the area measure (dA) for layered radiative transfer problems.

Problem specification

As shown in Fig. B.9, consider a heterogeneous medium in 3D with L homogeneous layers with each layer i being an infinitely large slab with thickness h_i and refractive index n_i. Note that the interfaces between adjacent layers are all *planar* and *parallel* to each other.

Consider a path ($P_0, \ldots, P_L$) with P_0 contained in Layer 1 and P_i being on the 'top' interface of Layer i (where $1 \leq i \leq L$). Here we assume the path satisfies Snell's law. Our goal is to find the ratio between the differential solid angle $d\sigma(\omega)$ around the ray (P_0, ω) with $\omega := (P_1 - P_0)/\|P_1 - P_0\|$ and the differential area $dA(P_L)$ around P_L on the 'top' interface of Layer L.
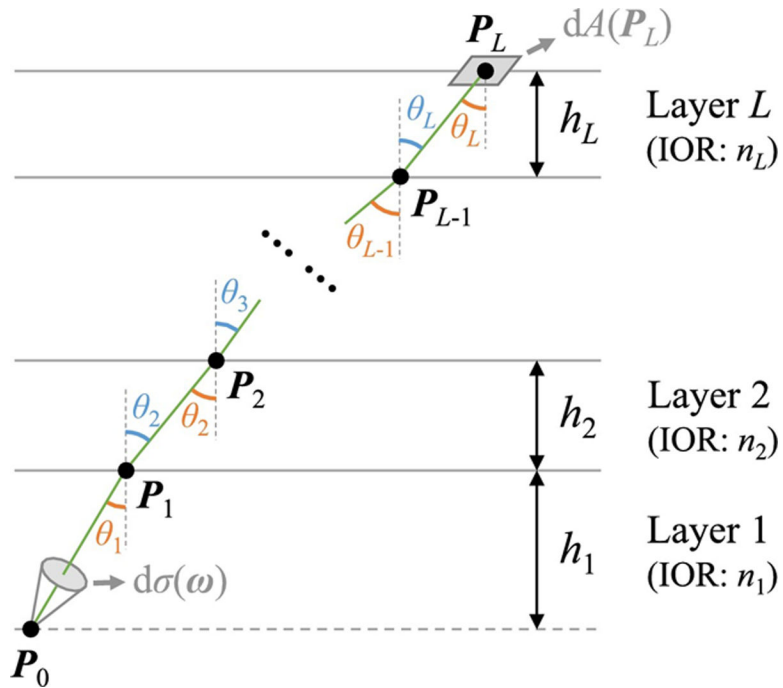

Fig. B.9. Problem specification.
Given a path (in green) connecting P_0 and P_L across multiple layers with varying indices of refraction (IOR), our goal is to derive the ratio between $dA(P_L)$ (under the area measure) and $d\sigma(\omega)$ (under the solid angle measure).
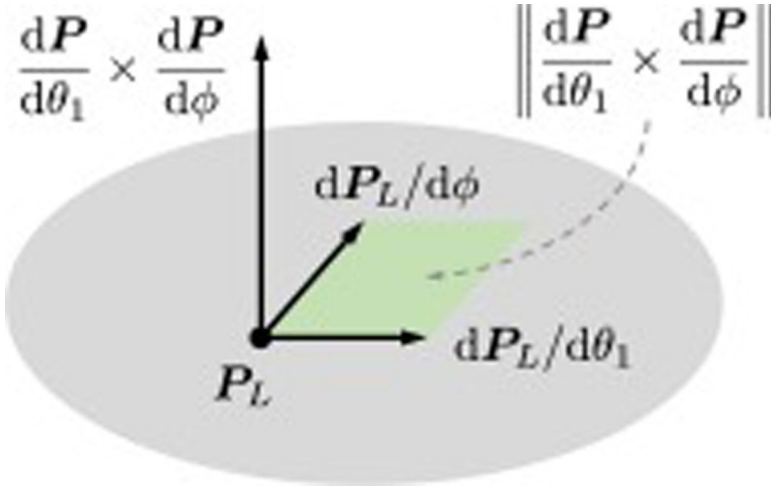
Fig. B.10. Change of variable:
$\mathrm{d}P_L/\mathrm{d}\theta_1$ and $\mathrm{d}P_L/\mathrm{d}\phi$ are two vectors within the tangent plane at P_L. The cross product $\mathrm{d}P_L/\mathrm{d}\theta_1 \times \mathrm{d}P_L/\mathrm{d}\phi$ is another vector orthogonal to both $\mathrm{d}P_L/\mathrm{d}\theta_1$ and $\mathrm{d}P_L/\mathrm{d}\phi$. The length of this vector product captures the area of the infinitesimal region shown in green.

Our derivation

Assume without loss of generality that

- P_0 locates at the origin $(0, 0, 0)$;

- The 'top' interface of Layer i (for all $1 \le i \le L$) is a plane perpendicular to the Z-axis with $z = \sum_{j=1}^{i} h_j$.

Given $\boldsymbol{\omega} = (\sin\theta_1\cos\phi, \sin\theta_1\sin\phi, \cos\theta_1)$, the whole path $(P_0, \ldots, P_L)$ can be uniquely determined by tracing a ray starting from $(P_0, \boldsymbol{\omega})$ and computing refracted directions via Snell's law. Thus, $P_1, \ldots, P_L$ can be considered as (vector-valued) functions of θ_1 and ϕ. In particular, it is easy to verify that

$$P_i = P_{i-1} + (\cos\phi\tan\theta_i h_i,\ \sin\phi\tan\theta_i h_i,\ h_i), \tag{B.1}$$

where θ_i denotes the angle between $(P_{i-1} - P_i)$ and the Z-axis (see Fig. B.9). Notice that, in our configuration, ϕ is preserved during refraction and remains identical for all i in Eq. (B.1).

By expanding Eq. (B.1), we have

$$P_i = \sum_{j=1}^{i} \left(\cos\phi\tan\theta_j h_j,\ \sin\phi\tan\theta_j h_j,\ h_j\right). \tag{B.2}$$

Then, it holds that (see Chapter 3 of the book by Gurtin [18])

$$\frac{\mathrm{d}A(\boldsymbol{P}_L)}{\mathrm{d}\theta_1\mathrm{d}\phi} = \left\|\frac{\mathrm{d}\boldsymbol{P}_L}{\mathrm{d}\theta_1} \times \frac{\mathrm{d}\boldsymbol{P}_L}{\mathrm{d}\phi}\right\|. \tag{B.3}$$

In Eq. (B.3), $\mathrm{d}\boldsymbol{P}_L/\mathrm{d}\theta_1$ and $\mathrm{d}\boldsymbol{P}_L/\mathrm{d}\phi$ are both 3-vectors, and the magnitude of their cross product indicates the size of an infinitesimal area around $\boldsymbol{P}_L$ (as illustrated in Fig. B.10). Previously, a similar approach has been used to compute the change-of-measure ratio for a two-layer problem in computer graphics [19].

We now derive a closed-form expression for the RHS of Eq. (B.3). Let

$$F(\theta_1) := \sum_{i=1}^{L} \tan\theta_i h_i. \tag{B.4}$$

Then, given Eq. (B.2) and Eq. (B.4), we have

$$\mathbf{P}_L = \left(F(\theta_1)\cos\phi,\ F(\theta_1)\sin\phi,\ \sum_{i=1}^{L} h_i\right). \tag{B.5}$$

As h_i is constant for all i, it holds that

$$\frac{\mathrm{d}\boldsymbol{P}_L}{\mathrm{d}\theta_1} = (F'(\theta_1)\cos\phi, F'(\theta_1)\sin\phi, 0),$$

$$\frac{\mathrm{d}\boldsymbol{P}_L}{\mathrm{d}\phi} = (-F(\theta_1)\sin\phi, F(\theta_1)\cos\phi, 0),$$

where $F' := \mathrm{d}F/\mathrm{d}\theta_1$. It follows that

$$\frac{d\boldsymbol{P}_L}{\mathrm{d}\theta_1} \times \frac{d\boldsymbol{P}_L}{\mathrm{d}\phi} = \left(0,\ 0,\ \cos^2\phi F(\theta_1)F'(\theta_1) + \sin^2\phi F(\theta_1)F'(\theta_1)\right)$$
$$= (0,\ 0,\ F(\theta_1)F'(\theta_1)).$$

Therefore,

$$\frac{\mathrm{d}A(\boldsymbol{P}_L)}{\mathrm{d}\theta_1\mathrm{d}\phi} = \left\|\frac{d\boldsymbol{P}_L}{\mathrm{d}\theta_1} \times \frac{d\boldsymbol{P}_L}{\mathrm{d}\phi}\right\| = F(\theta_1)F'(\theta_1). \tag{B.6}$$

Since $\mathrm{d}\sigma(\boldsymbol{\omega}) = \sin\theta_1\mathrm{d}\theta_1\mathrm{d}\phi$, we have

$$\frac{\mathrm{d}A(\boldsymbol{P}_L)}{\mathrm{d}\sigma(\boldsymbol{\omega})} = \frac{F(\theta_1)F'(\theta_1)}{\sin\theta_1}. \tag{B.7}$$

At this point, the only remaining task is to obtain F' (by differentiating F):

$$F'(\theta_1) = \frac{\mathrm{d}}{\mathrm{d}\theta_1} \sum_{i=1}^{L} \tan\theta_i h_i = \sum_{i=1}^{L} \left(\frac{\mathrm{d}}{\mathrm{d}\theta_1} \tan\theta_i h_i \right) = \sum_{i=1}^{L} \frac{h_i}{\cos^2\theta_i} \frac{\mathrm{d}\theta_i}{\mathrm{d}\theta_1} . \tag{B.8}$$

According to Snell's law, $n_i \sin\theta_i = n_{i-1} \sin\theta_{i-1}$ for all $1 < i \le L$. It follows that

$$\sin\theta_i = \frac{n_{i-1}}{n_i}\sin\theta_{i-1} = \frac{n_{i-1}}{n_i}\frac{n_{i-2}}{n_{i-1}}\sin\theta_{i-2} = \cdots = \left(\prod_{j=1}^{i-1} \frac{n_j}{n_{j+1}} \right) \sin\theta_1 = \eta_i \sin\theta_1,$$

where $\eta_i := n_1/n_i$. Then, $\theta_i = \arcsin(\eta_i \sin\theta_1)$ and

$$\frac{\mathrm{d}\theta_i}{\mathrm{d}\theta_1} = \frac{\eta_i\cos\theta_1}{\sqrt{1 - \eta^2\sin^2\theta_1}} = \eta_i\frac{\cos\theta_1}{\cos\theta_i} . \tag{B.9}$$

Combining Eq. (B.8) and Eq. (B.9) yields

$$F'(\theta_1) = \sum_{i=1}^{L} \eta_i h_i \frac{\cos\theta_1}{\cos^3\theta_i} . \tag{B.10}$$

We now derive an alternative form of Eq. (B.7) that directly depends on angles (θ_i) and refractive indices (n_i) illustrated in Fig. B.9. Let $D_i := \|\boldsymbol{P}_i - \boldsymbol{P}_{i-1}\|$. Then, it holds that

$$\frac{F(\theta_1)}{\sin\theta_1} = \sum_{i=1}^{L} \frac{\tan\theta_i h_i}{\sin\theta_1} = \sum_{i=1}^{L} \frac{\sin\theta_i}{\sin\theta_1} \frac{h_i}{\cos\theta_i} = \sum_{i=1}^{L} \eta_i D_i, \tag{B.11}$$

and

$$\begin{aligned}
F'(\theta_1) &= \frac{1}{\cos\theta_L}(\cos\theta_L F'(\theta_1)) \\
&= \frac{1}{\cos\theta_L} \sum_{i=1}^{L} \eta_i \frac{h_i}{\cos\theta_i} \frac{\cos\theta_1\cos\theta_L}{\cos^2\theta_i} \\
&= \frac{1}{\cos\theta_L} \sum_{i=1}^{L} \eta_i D_i \frac{\cos\theta_1\cos\theta_L}{\cos^2\theta_i} .
\end{aligned} \tag{B.12}$$

Due to Eqs. (B.7), (B.11), (B.12), we have

$$\frac{\mathrm{d}A(\boldsymbol{P}_L)}{\mathrm{d}\sigma(\boldsymbol{\omega})} = \frac{F(\theta_1)F'(\theta_1)}{\sin\theta_1} = \frac{1}{\cos\theta_L} \left(\sum_{i=1}^{L} \eta_i D_i \right) \left(\sum_{i=1}^{L} \eta_i D_i \frac{\cos\theta_1\cos\theta_L}{\cos^2\theta_i} \right) . \tag{B.13}$$

B.1. Special cases

Single layer

When there is only one layer (i.e., $L = 1$), since $\eta_1 := n_1/n_1 \equiv 1$, Eq. (B.13) reduces to

$$\frac{\mathrm{d}A(\boldsymbol{P}_1)}{\mathrm{d}\sigma(\boldsymbol{\omega})} = \frac{1}{\cos\theta_1}D_1D_1 = \frac{D_1^2}{\cos\theta_1}, \tag{B.14}$$

matching the standard ratio between the measures of area and solid angle.

Double layer

When $L = 2$, Eq. (B.13) reduces to

$$\frac{\mathrm{d}A(\boldsymbol{P}_1)}{\mathrm{d}\sigma(\boldsymbol{\omega})} = \frac{1}{\cos\theta_2}(D1 + \eta_2 D_2)\left(\frac{\cos\theta_2}{\cos\theta_1}D_1 + \frac{\cos\theta_1}{\cos\theta_2}\eta_2 D_2\right). \tag{B.15}$$

This equation was introduced previously by Walter et al. [19] (see Eq. (18) in their paper).

References

[1]. Spanier J, Gelbard EM, Monte Carlo Principles and Neutron Transport Problems, Addison-Wesley, 1969.

[2]. Kong R, Spanier J, Transport-constrained extensions of collision and track length estimators for solutions of radiative transport problems, J. Comput. Phys. 242 (2013) 682–695. [PubMed: 24058206]

[3]. Hayakawa CK, Spanier J, Venugopalan V, Comparative analysis of discrete and continuous absorption weighting estimators used in Monte Carlo simulations of radiative transport in turbid media, JOSA A 31 (2) (2014) 301–311. [PubMed: 24562029]

[4]. Booth TE, Pederson SP, Unbiased combinations of nonanalog Monte Carlo techniques and fair games, Nucl. Sci. Eng. 110 (3) (1992) 254–261.

[5]. Chandrasekhar S, Radiative Transfer, Courier Corporation, 1960.

[6]. Lux I, Koblinger L, Monte Carlo Particle Transport Methods: Neutron and Photon Calculations, CRC Press, 1991.

[7]. Hammersley JM, Handscomb DC, Monte Carlo Methods, Methuen, 1964.

[8]. Case KM, Zweifel PF, Linear Transport Theory, Addison-Wesley, 1967.

[9]. Davison B, Sykes JB, Neutron Transport Theory, Clarendon Press, 1957.

[10]. Veach E, Robust Monte Carlo methods for light transport simulation, No. 1610, Stanford University PhD thesis, 1997.

[11]. Pauly M, Kollig T, Keller A, Metropolis light transport for participating media, in: Rendering Techniques 2000, Springer, 2000, pp. 11–22.

[12]. Werner CJ, Bull JS, Solomon CJ, Brown FB, McKinney GW, Rising ME, Dixon DA, Martz RL, Hughes HG, Cox LJ, Zukaitis AJ, Armstrong JC, Forster RA, Casswell L, MCNP version 6.2 release notes, 2018.

[13]. Zhao S, Kong R, Spanier J, Towards real-time Monte Carlo for biomedicine, in: International Conference on Monte Carlo and Quasi-Monte Carlo Methods in Scientific Computing, Springer, 2016, pp. 447–463.

[14]. Wang L, Jacques SL, Zheng L, MCML—Monte Carlo modeling of light transport in multi-layered tissues, Comput. Methods Programs Biomed. 47 (2) (1995) 131–146. [PubMed: 7587160]

[15]. Collier T, Arifler D, Malpica A, Follen M, Richards-Kortum R, Determination of epithelial tissue scattering coefficient using confocal microscopy, IEEE J. Sel. Top. Quantum Electron. 9 (2) (2003) 307–313.

[16]. Walker D, Brown B, Blackett A, Tidy J, Smallwood R, A study of the morphological parameters of cervical squamous epithelium, Physiol. Meas. 24 (1) (2003) 121. [PubMed: 12636191]

[17]. Chang VT-C, Cartwright PS, Bean SM, Palmer GM, Bentley RC, Ramanujam N, Quantitative physiology of the precancerous cervix in vivo through optical spectroscopy, Neoplasia 11 (4) (2009) 325–332. [PubMed: 19308287]

[18]. Gurtin ME, An Introduction to Continuum Mechanics, Academic Press, 1981.

[19]. Walter B, Zhao S, Holzschuch N, Bala K, Single scattering in refractive media with triangle mesh boundaries, ACM Trans. Graph. 28 (3) (2009) 92.
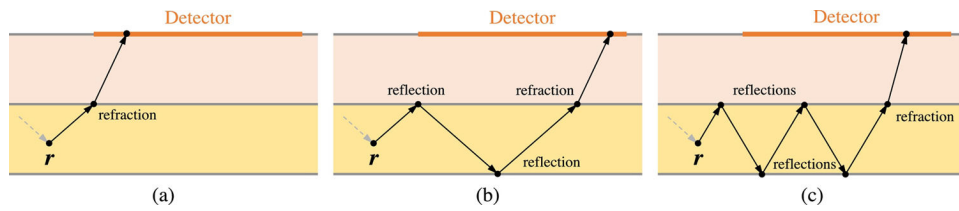
Fig. 1. Extended next-event estimations:

after a photon enters a collision at *r*, there exist infinitely many ways for it to reach the detector via only interfacial reflections and refractions. For example, in (a), the photon (after leaving *r*) undergoes one refraction before reaching the detector; in (b), the photon is reflected twice and then refracted; in (c), the connection from *r* to the detector involves four reflections and one refraction.
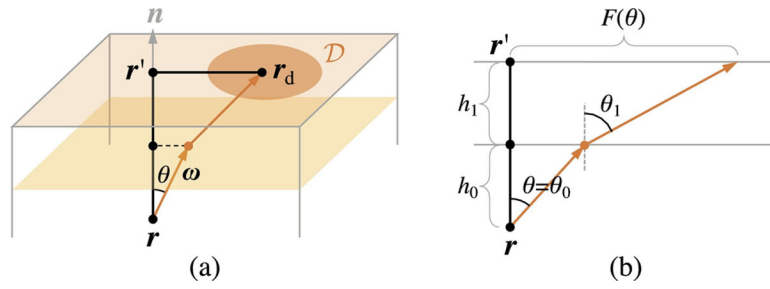
Fig. 2. Extended next-event connection:

(a) Provided an internal location r and an interfacial location $r_d \in \mathcal{D}$, the direction ω that allows the extension of a light ray originated at (r, ω) to go through r_d always lies within the plane given by r, r_d, and n. (b) The search for ω amounts to finding a proper angle θ with $F(\theta) = \|r' - r_d\|$.
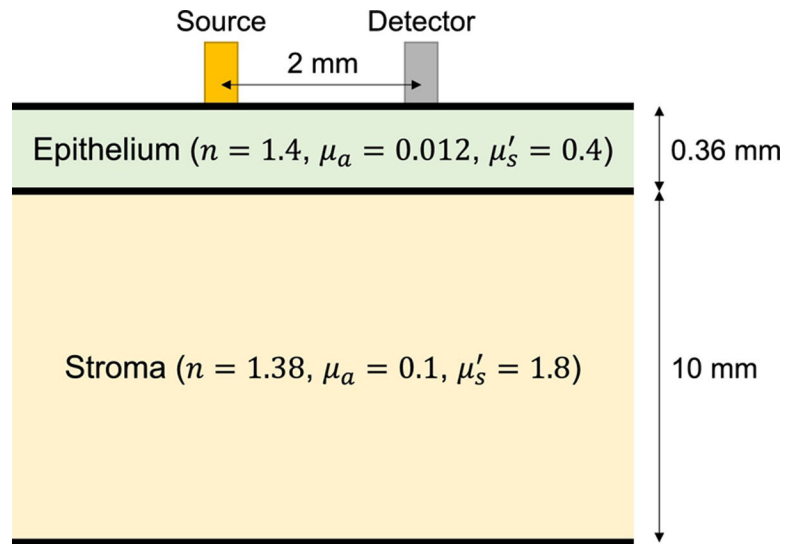
Fig. 3.
We use a **layered configuration** with layer optical properties modeled according to prior works [15–17].
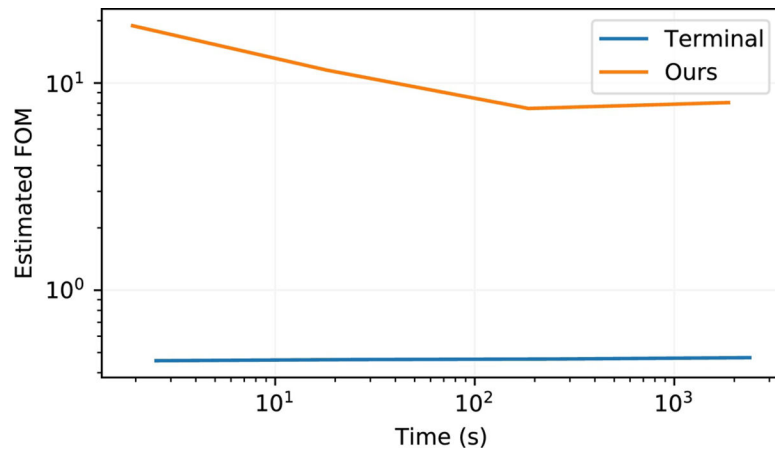
Fig. 4.
Figure of merit (FOM) of the terminal and our hybrid estimators applied to the two-layer problem (to compute the flux received by the detector). When computing the FOM values using Eq. (1), the σ^2 term is approximated using sample variance. Under this metric, the efficiency of our technique is over an order of magnitude greater than that of the terminal estimator.
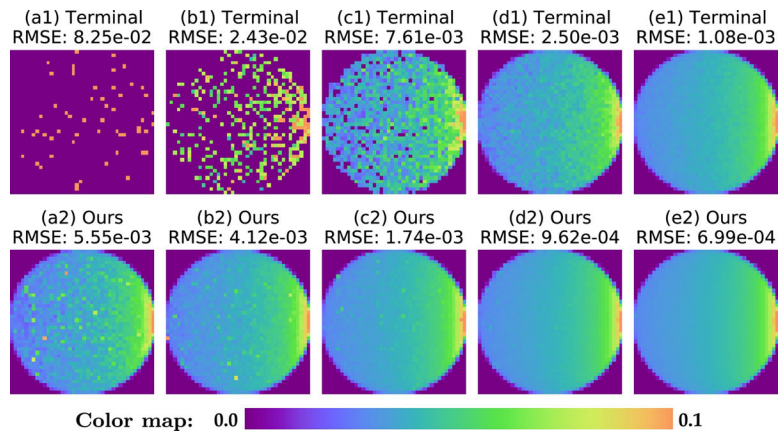
(a1) Terminal RMSE: 8.25e-02 (b1) Terminal RMSE: 2.43e-02 (c1) Terminal RMSE: 7.61e-03 (d1) Terminal RMSE: 2.50e-03 (e1) Terminal RMSE: 1.08e-03

(a2) Ours RMSE: 5.55e-03 (b2) Ours RMSE: 4.12e-03 (c2) Ours RMSE: 1.74e-03 (d2) Ours RMSE: 9.62e-04 (e2) Ours RMSE: 6.99e-04

Color map: 0.0 █ 0.1

Fig. 5.

Intensity received by the detector in the two-layer problem from varying directions estimated with the terminal estimator (a1–e1) and our approach (a2–e2). Both estimators run in roughly the same time for each column. Our hybrid estimator is able to produce much cleaner results thanks to our extended next-event estimation depicted in §4.2.
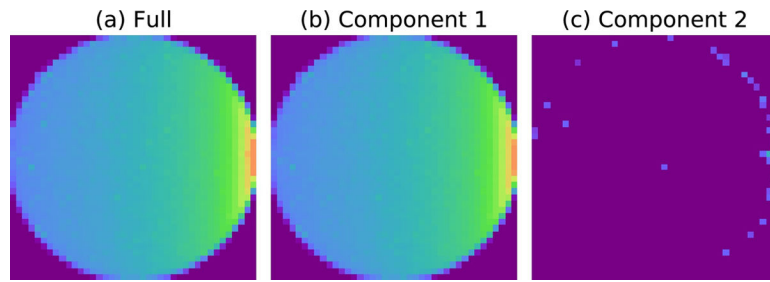
Fig. 6. Per-component visualization:

(a) Estimated intensity (same as Figure 5–d2); (b) The component handled by our extended next-event estimator for biographies from $\mathscr{B}_1$; (c) The other component handled using terminal for biographies from $\mathscr{B}_2$.
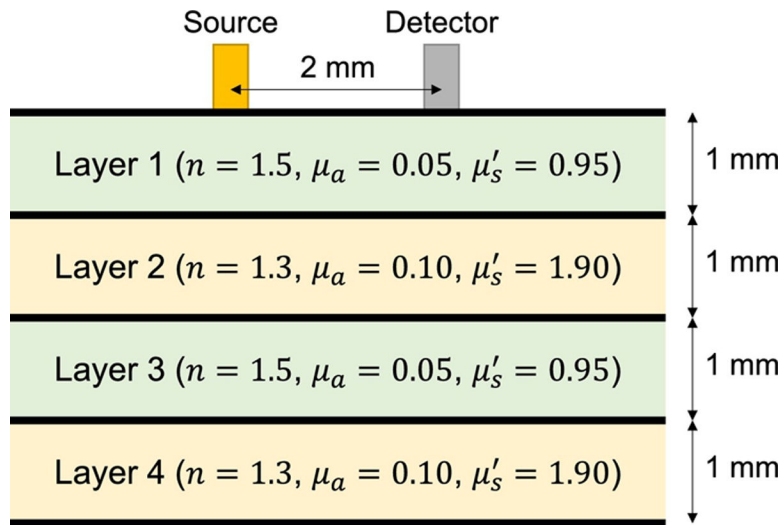
Fig. 7.
We use a **synthetic four-layer configuration** to demonstrate the capability of our technique for handling media with more than two layers.
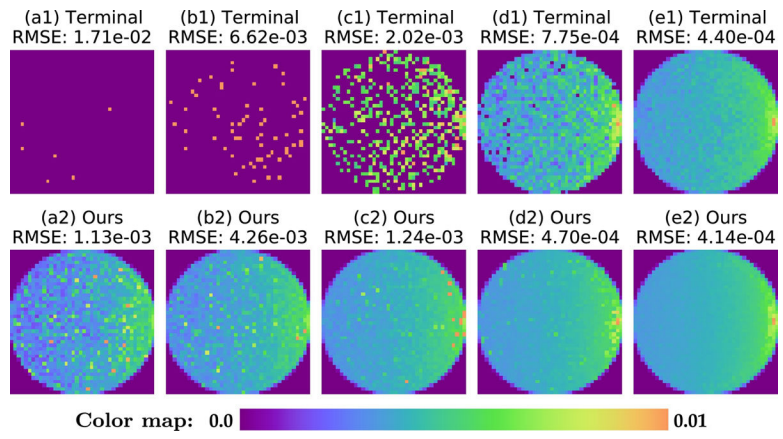
Fig. 8.

Intensity received by the detector in the four-layer problem from varying directions estimated with the terminal estimator (a1–e1) and our approach (a2–e2) at equal time per column.